Materials Chemistry and Physics 133 (2012) 876–883

Contents lists available at SciVerse ScienceDirect

Materials Chemistry and Physics

journal homepage: www.elsevier.com/locate/matchemphys

Structural, EPR, photo and thermoluminescence properties of ZnO:Fe nanoparticles

A. Jagannatha Reddy[a], M.K. Kokila[b], H. Nagabhushana[c,*], S.C. Sharma[c], J.L. Rao[d], C. Shivakumara[e], B.M. Nagabhushana[f], R.P.S. Chakradhar[g,*]

[a] Department of Physics, M. S. Ramaiah Institute of Technology, Bangalore 560 054, India
[b] Department of Physics, Bangalore University, Bangalore 560 056, India
[c] Prof C.N.R. Rao Centre for Nano Research, Tumkur University, Tumkur 572 103, India
[d] Department of Physics, S.V. University, Tirupathi 517 502, India
[e] Solid State and Structural Chemistry Unit, Indian Institute of Science, Bangalore 560 012, India
[f] Department of Chemistry, M. S. Ramaih Institute of Technology, Bangalore 560 054, India
[g] CSIR-National Aerospace Laboratories, Bangalore 560017, India

ARTICLE INFO

Article history:
Received 28 July 2011
Received in revised form 26 January 2012
Accepted 29 January 2012

Keywords:
A. Nanostructures
B. Chemical synthesis
C. Electron microscopy
D. Luminescence
D. Crystal structure

ABSTRACT

$Zn_{(1-x)}Fe_{(x)}O_{(1+0.5x)}$ ($x = 0.5–5$ mol%) nanoparticles were synthesized by a low temperature solution combustion route. The structural characterization of these nanoparticles by PXRD, SEM and TEM confirmed the phase purity of the samples and indicated a reduction in the particle size with increase in Fe content. A small increase in micro strain in the Fe doped nanocrystals is observed from W–H plots. EPR spectrum exhibits an intense resonance signal with effective g values at $g \approx 2.0$ with a sextet hyperfine structure (hfs) besides a weak signal at $g \approx 4.13$. The signal at $g \approx 2.0$ with a sextet hyperfine structure might be due to manganese impurity where as the resonance signal at $g \approx 4.13$ is due to iron. The optical band gap E_g was found to decrease with increase of Fe content. Raman spectra exhibit two non-polar optical phonon (E_2) modes at low and high frequencies at 100 and 435 cm^{-1} in Fe doped samples. These modes broaden and disappear with increase of Fe dopant concentration. TL measurements of γ-irradiated (1–5 kGy) samples show a main glow peak at 368 °C at a warming rate of 6.7 °Cs^{-1}. The thermal activation parameters were estimated from Glow peak shape method. The average activation energy was found to be in the range 0.34–2.81 eV.

1. Introduction

Research on nanometer-sized materials has increased remarkably during the past years due to their unique characteristics termed quantum confinement effects. The term, quantum confinement effect, was introduced to explain a wide range of mechanical, electrical and optical properties of nano-sized materials in response to changes in dimensions or shapes within nano-scales [1,2]. ZnO with a wide energy band-gap (3.27 eV) in bulk is one of the II–VI semiconductor materials, making it attractive for the nanoelectronic and photonic applications. Its advantages over other materials for electronic applications lie in a high exciton binding energy (60 meV), breakdown strength and its multifunctional behavior when suitably doped [3]. Each atom of Zn is surrounded by four atoms of oxygen in tetrahedral coordination in ZnO wurtzite structure. ZnO is ready for applications in UV-emitting diodes, cathode-ray phosphors, transparent conductors, varistors, chemical sensors, UV-protection films, and ultra fast nonlinear optical devices [4,5].

Fe doped ZnO systems have attracted much attention because of predictions that it is ferromagnetic with a high Curie temperature above 300 K [6]. The presence of TM ions in the host semiconductor leads to an exchange interaction between itinerant sp-band electrons or holes and the d-electron spins localized at the magnetic ions, resulting in versatile magnetic field induced functionalities. A number of investigations on the synthesis of ZnO nanoparticles have been reported in the literature including thermal decomposition, chemical vapor deposition, sol–gel, hydrothermal, spray pyrolysis, precipitation, vapor phase oxidation, thermal vapor transport and condensation [7–12]. Low temperature solution combustion synthesis is emerging as a promising technique for the preparation of nanopowders as it is simple, fast and cost effective, does not require high-temperature furnaces and complicated set-ups [13]. In the present study, Fe doped (0.5–5 mol%) ZnO nanoparticles are synthesized by a low temperature

* Corresponding authors. Tel.: +91 9945954010.
E-mail addresses: bhushanvl@rediffmail.com (H. Nagabhushana), sreechakra72@yahoo.com (R.P.S. Chakradhar).

0254-0584/$ – see front matter © 2012 Elsevier B.V. All rights reserved.
doi:10.1016/j.matchemphys.2012.01.111

solution combustion route. The synthesized nanopowders are well characterized by using Powder X-ray diffraction (PXRD), scanning electron microscopy (SEM), transmission electron microscopy (TEM), Fourier transform infrared (FTIR) spectroscopy. The electron paramagnetic resonance (EPR) spectroscopy has been used to study the oxidation states, types of coordination and geometry of the ligand sites. In addition, UV–vis, photo and thermoluminescent properties were also investigated.

2. Experimental

2.1. Synthesis

Zinc nitrate ($Zn(NO_3)_26H_2O$) was used as oxidizer, oxalyl dihydrazide (ODH) [$C_2H_6N_4O_2$] was used as fuel and $Fe(NO_3)_3$ as a dopant. The oxidizer to fuel ratio was calculated based on oxidizing (O) and fuel (F) valencies of the reactants, keeping O/F = 1. The starting materials were mixed in petri dish with minimum quantity of de-ionized water to form a solution. The dish was then transferred into a preheated furnace maintained at 300 ± 10 °C. Initially, the paste melted and underwent dehydration followed by decomposition with the evolution of large amounts of gases. The mixture frothed and swells, forming foam, which ruptured with a flame and glowed to incandescence. During incandescence, the foam further swells to the capacity of the container. The entire combustion process was over in less than 5 min.

2.2. Instruments used

The powder X-ray diffraction studies were carried out using PANalytical X'pert Pro, Almelo (The Netherlands) with Cu Kα radiation (λ = 1.541 Å). The surface morphology of the samples was examined using Scanning electron microscopy (JEOL JSM 840A) by sputtering technique with gold as covering contrast material. Transmission Electron Microscopy (TEM) analysis was performed on a Hitachi H-8100 (accelerating voltage up to 200 kV, LaB_6 filament) equipped with EDS (Kevex Sigma TM Quasar, USA). FTIR spectrum was taken using a Perkin-Elmer Rx1 instrument. The UV–vis spectrum was recorded on a UV-3101 Shimadzu Visible spectrophotometer. The photoluminescence studies were carried out using a Perkin-Elmer LS-55 luminescence spectrophotometer equipped with Xe lamp. Raman studies were carried out on Renishaw In-via Raman spectrometer with 633 nm He–Cd laser and a Leica DMLM optical microscope equipped with 50X objective, thus providing a laser spot of 2 μm in diameter. A powdered specimen of 100 mg was taken in a quartz tube for EPR measurements. The synthesized samples were irradiated with different doses of γ-rays in the range 1–5 kGy from Co-60 source at room temperature. After the desired exposure, TL glow curves were recorded on a Nucleonics TLD reader taking 5 mg of the sample each time at a heating rate of 6.7 °C s^{-1}. The EPR spectrum was recorded at room temperature using a JEOL-FE-1X EPR spectrometer operating in the X-band frequency (≈9.205 GHz) with a field modulation frequency of 100 kHz. The magnetic field was scanned from 0 to 500 mT and the microwave power used was 10 mW.

3. Results and discussion

3.1. Powder X-ray diffraction studies (PXRD)

The crystal structure of synthesized samples has been investigated using Powder X-ray diffraction (PXRD). Fig. 1 shows PXRD patterns of undoped and Fe doped (0.5–5 mol%) ZnO nanoparticles. All the diffraction peaks of undoped and doped ZnO samples are indexed to wurtzite hexagonal structure (JCPDS No.36-1451). A

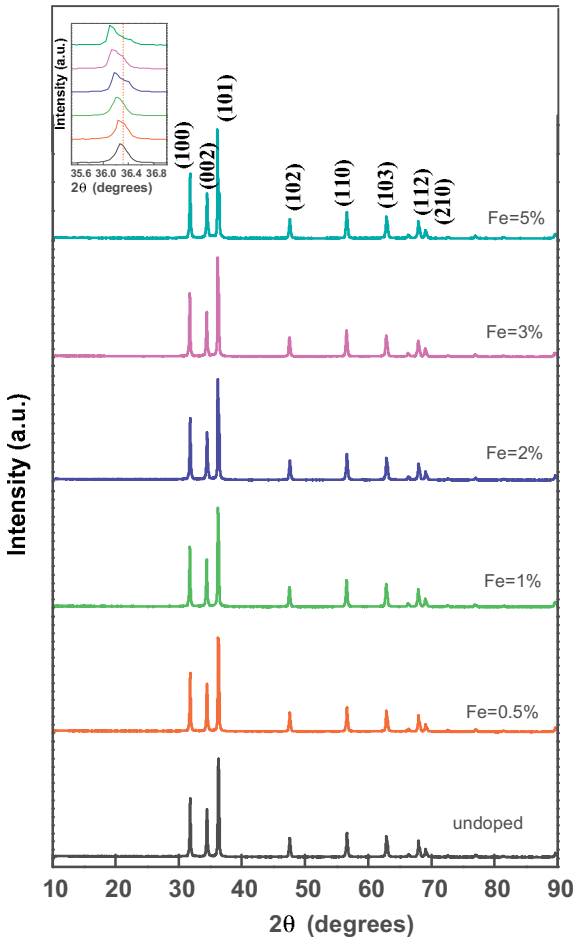

Fig. 1. PXRD patterns of un-doped and Fe doped ZnO (inset: shift in peaks).

small shift in the position of main peak (1 0 1) to the lower side of 2θ values is observed for Fe doped samples (Inset of Fig. 1). The shift of XRD peaks of Fe-doped nanoparticles indicates that Zn cations have been successfully substituted with bigger Fe cations. This observation is similar to the case in transition metal (Mn, Cu and Ni) doped ZnO [14]. The peaks are found to be broadened with increase of concentration of Fe^{3+} ion in ZnO. This has been explained as due to reduction of grain size and development of strain in ZnO lattice with incorporation of Fe^{3+} ions. No other peaks related to Fe compounds were found. It suggests that Fe^{3+} ions occupy Zn^{2+} sites or interstitial sites in the ZnO lattice without changing the wurtzite structure.

The accurate unit cell parameters of various compositions of ZnO:Fe were determined by Rietveld refinement of the observed diffraction profile using Fullprof software [15]. The pseudo-voigt peak profile function was used and the background was approximated by linear interpolation between a set of background points with refinable heights. The fitted and observed data along with the difference between them are shown in Fig. 2. The obtained reliability factors R_p, R_{wp}, R_{Bragg}, χ^2, R_F and lattice parameters calculated from the Rietveld refinement are tabulated in Table 1. Very little change was found in the lattice parameters of doped ZnO which may be due to low doping concentration of Fe in the ZnO matrix.

In order to study the effect of Fe concentration on crystallite size, the average crystallite size was estimated from the Debye–Scherrer's equation:

$$D = \frac{k\lambda}{\beta \cos \theta} \quad (1)$$

Table 1
Rietveld refinement results of Fe doped ZnO nanoparticles.

Fe conc. (mol%)	Lattice parameters		Volume of unit cell (Å)^3	R_p	R_{wp}	χ^2	R_{Bragg}	R_F
	a (nm)	c (nm)						
0	3.251 (2)	5.207 (3)	47.65 (5)	4.08	5.40	1.40	2.85	1.96
0.5	3.251 (2)	5.207 (3)	47.67 (4)	5.69	7.90	1.06	4.27	2.80
1	3.252 (1)	5.207 (2)	47.68 (4)	5.56	7.57	0.966	2.16	1.99
2	3.252 (2)	5.206 (3)	47.69 (5)	5.68	7.89	1.01	2.98	2.45
3	3.252 (1)	5.206 (2)	47.68 (5)	5.83	8.08	1.08	2.28	1.97
5	3.254 (2)	5.207 (3)	47.70 (5)	6.32	8.83	1.26	2.80	2.10

Atom	Oxidation state	Wyckoff notation	x	y	z	Occupancy
Zn	+2	2b	0.3333	0.6666	0.0000	0.95
Fe	+3	2b	0.3333	0.6666	0.0000	0.05
O	−2	2b	0.3333	0.6666	0.3798	1

where β is FWHM (rad), λ is wavelength of X-rays, θ is glancing angle, k is a constant that depends on the grain shape (0.9 for circular grains). A decrease in the particle size from 42 nm to 34 nm was found with increase of Fe concentration (Fig. 3). This has been explained as due to development of strain in ZnO lattice with incorporation of Fe^{3+} ions. We have estimated and compared the lattice strains in undoped and Fe doped ZnO nanoparticles using the Williamson–Hall (W–H) equation [16],

$$\beta \cos\theta = \frac{k\lambda}{D} + 4\varepsilon \sin\theta \quad (2)$$

where ε is the strain associated with the nanoparticles. Eq. (2) represents a straight line between 4 sinθ (X-axis) and $\beta\cos\theta$ (Y-axis). The slope of line gives the strain (ε) and intercept ($k\lambda/D$) of this line on Y-axis gives crystallite size (D). Fig. 4 shows the W–H plots of undoped and Fe doped ZnO samples. The calculated values of D from W–H plots and Scherer's formula and the corresponding strains for different Fe doping concentration in ZnO are presented in Table 2.

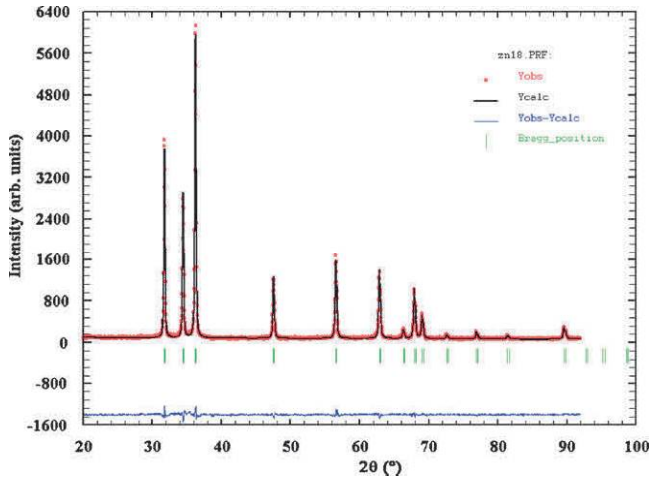

Fig. 2. Reitveld refinement of PXRD pattern of Fe doped ZnO.

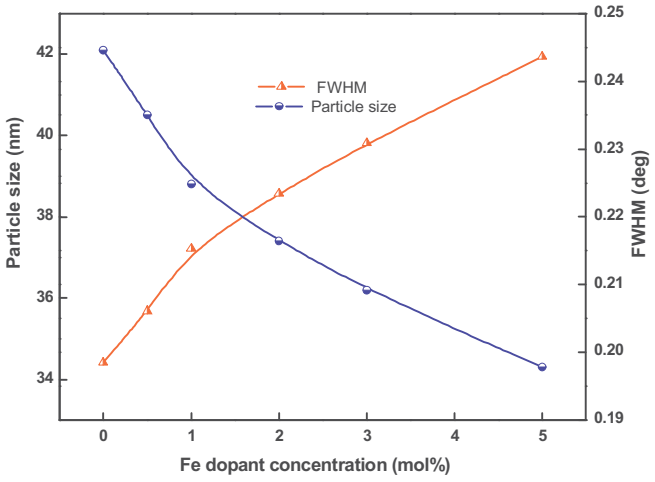

Fig. 3. Variation of particle size and FWHM with Fe dopant concentration.

3.2. Microstructure

Fig. 5 shows the SEM images of the Fe doped ZnO nanoparticles with low- and high-magnification. High-resolution SEM images show the presence of several nanoparticles within the grains. During the combustion process, several gases are evolved and hence the combustion product is porous as shown in the micrographs but the porosity levels of 0.5 mol% Fe doped ZnO sample is much lower compared to high mol% Fe doped samples. The micrograph of 0.5 mol% Fe doped sample (Fig. 5a) show the presence of bunches of small particles on the surface of angular plates and a further higher magnification (Fig. 5b) resolved the nearly hexagonal angular shape platelet particles with various sizes. With increase in Fe dopant concentration, the powders become more porous as is evident from Fig. 5c and d. The 5 mol% Fe doped powder shows honeycomb structure with lots of voids and pores formed by the escaping gases during combustion as is indicated in Fig. 5e and f. These porous powders are highly friable which facilitates easy grinding to obtain finer particles. Fig. 6 shows the transmission electron microscopy

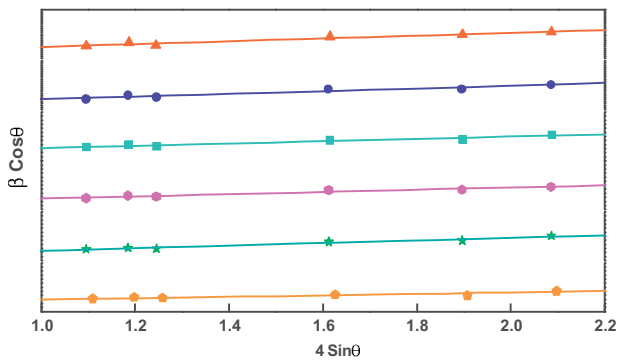

Fig. 4. W–H plots of Fe doped ZnO nanopowder.

Table 2
Estimated values of crystallite size (D) by W–H plots, Scherer's formula and strains for different Fe (0.5–5 mol%) doping concentration in ZnO.

Fe conc. (mol%)	Crystallite size (nm) by Scherrer's formula	Crystallite size (nm) from W–H plot	Strain × 10^{-4}
0	42.8	41.9	8.4
0.5	40.5	41.0	9.8
1	38.8	38.3	10.6
2	37.4	36.9	11.5
3	36.2	36.0	13.7
5	34.3	35.1	14.8

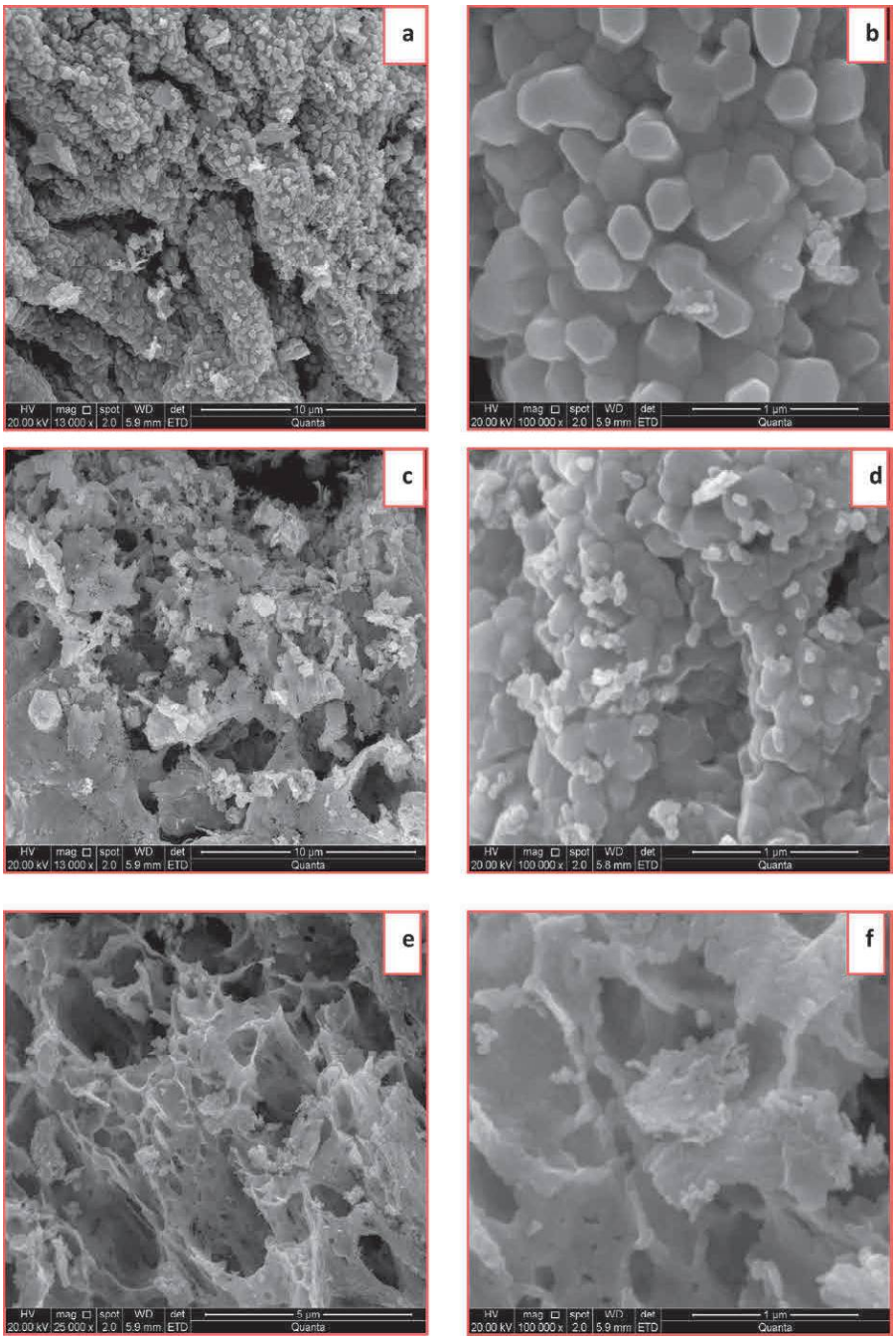

Fig. 5. SEM images of 0.5 mol% (a and b), 2 mol% (c and d) and 5 mol% (e and f) Fe doped ZnO nanopowder.

(TEM) image of ZnO nanoparticles showing the similar morphology as that of the SEM observations. The corresponding selected area electron diffraction (SAED) (inset Fig. 6) pattern indicates that the nanoparticles are wurtzite single crystalline in nature without dislocations and stacking faults.

3.3. Fourier transformed Infrared spectroscopy (FTIR)

The characteristic FTIR spectrum of the undoped and Fe doped ZnO nanoparticles are depicted in Fig. 7. The peak at 418 cm^{-1} is ascribed to Zn–O stretching vibration [17]. A weak absorption band

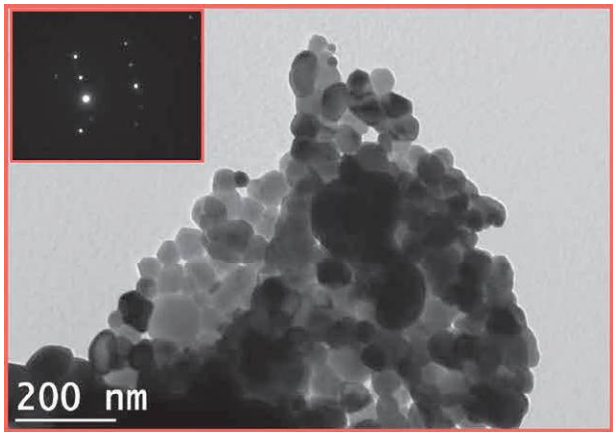

Fig. 6. TEM image of ZnO nanopowder.

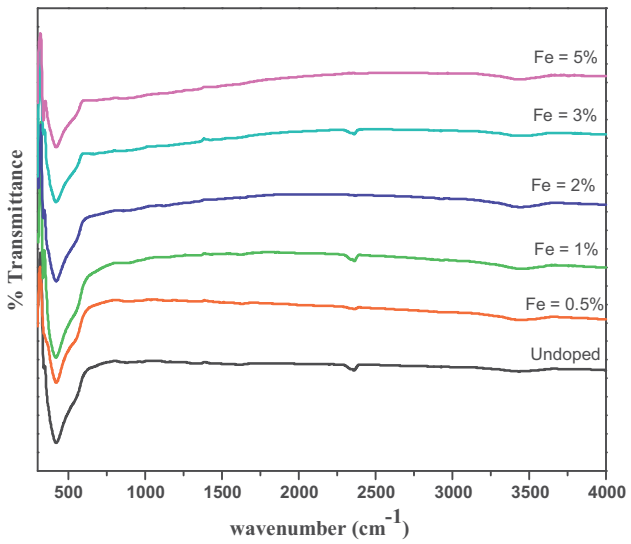

Fig. 7. FTIR spectra of Fe doped ZnO nanopowder.

at 3427 cm^{-1} indicated the presence of hydroxyl-groups, which is probably due to water re-adsorption from the ambient atmosphere. After introducing iron ion in the host, the intensity of the absorption peak at 418 cm^{-1} decreased slightly, this might be due to better crystallinity of the compound.

3.4. Raman spectroscopy

To see the effect of Fe doping on ZnO symmetry and vibrational modes, Raman studies were carried out and the spectrum is shown in Fig. 8. ZnO has hexagonal Wurtzite structure, with space group of $P6_3mc$ along with two formula units per primitive cell. According to group theory there exist eight sets of the zone center optical phonons and can be represented as

$$\Gamma_{opt} = A_1 + E_1 + 2E_2 \quad (3)$$

The Raman active phonons of A_1 and E_1 symmetry are polar phonons, whereas phonons of E_2 symmetry are non-polar. Polar modes can be split into transverse (TO) and longitudinal (LO) optical phonons exhibiting different wavenumbers [18]. In case of non-polar Raman active phonon modes, E_2 can have two wavenumbers (E_2 low) and (E_2 high). The active modes near 100, 438, 332 and 580 cm^{-1} appeared in Raman spectra corresponds to ZnO. The peaks at 100 and 438 cm^{-1} in undoped ZnO corresponds to two

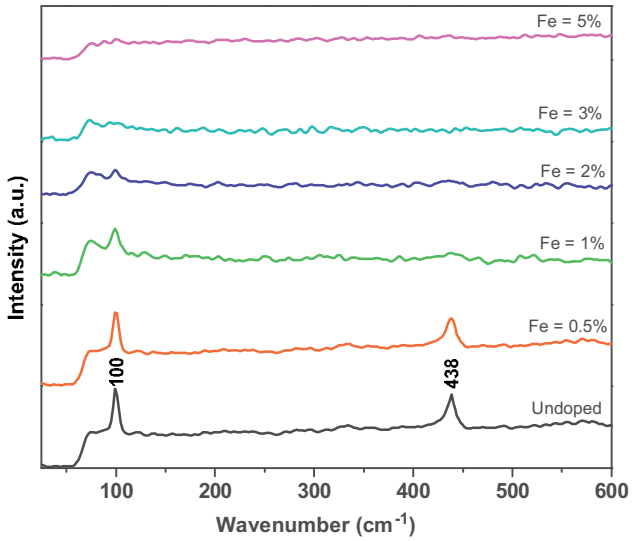

Fig. 8. Raman spectrum of Fe doped ZnO nanopowder.

non-polar optical phonon (E_2) modes at low and high frequencies respectively which are characteristic peaks of Wurtzite structure.

It should be noted that the intensity of 100 cm^{-1} (E_2) peak decreases and becomes broad with increase of Fe dopant and almost disappears for 5 mol% Fe doped ZnO. It is further observed that the E_2 (high) 438 cm^{-1} mode is broadened and shifted to 435 cm^{-1} in case of 0.5 mol% Fe doped ZnO. With further increase in Fe dopant concentration, the E_2 (high) mode disappears. The small shifting of E_2 phonon mode can be related to a strain induced by Fe dopant. Same phenomenon occurred in Ce and Tb doped ZnO samples reported in literature [19,20]. When the size of particles reduces to nanoscale, the $k = 0$ selection rule for the first order Raman scattering is relaxed and the phonon scattering will not be limited to the centre of Brillouin zone. Hence the phonon dispersion near the centre of the Brillouin zone should be considered as well. As a result, the shift and broadening of first order optical phonon scattering modes are observed.

Sofer et al. [21] studied Raman spectra of transition metal ion doped (Mn, Fe, Co) ZnO by flux growth. An intense peak of E_2 phonon mode was observed at 437 cm^{-1} and is slightly shifted in Fe and Co doped samples when compared to pure ZnO. Further, enhancement of A_1 (LO) phonon mode in transition metal ion doped ZnO is related to deep level free electron traps created by these dopants. The vibrational modes observed around 500 and 520 cm^{-1} are related to defect activated Raman scattering phonon modes (DARS). They might be associated with oxygen and zinc vacancies, interstitials and other defects induced by transition metal ions.

3.5. UV–visible absorption spectrum

The UV–visible absorption spectra of undoped and Fe doped samples are shown in Fig. 9. A small blue shift in absorption edges is observed for the Fe doped samples. The direct energy band gap for the undoped and Fe doped ZnO nanoparticles was estimated by fitting the absorption data to the direct transition equation,

$$(\alpha h\nu)^2 = A(h\nu - E_g) \quad (4)$$

where, 'α' is optical absorption co-efficient, ($h\nu$) is the photon energy, E_g is the direct band gap and 'A' is a constant. Plotting $(\alpha h\nu)^2$ as a function of photon energy and extrapolating linear portion of the curve to the photon energy axis as shown in Fig. 10, the energy gap (E_g) of Fe doped ZnO nanoparticles is found to be 3.27, 3.24, 3.20, 3.13, 3.08 and 3.04 eV for undoped and 0.5, 1, 2, 3 and 5 mol%

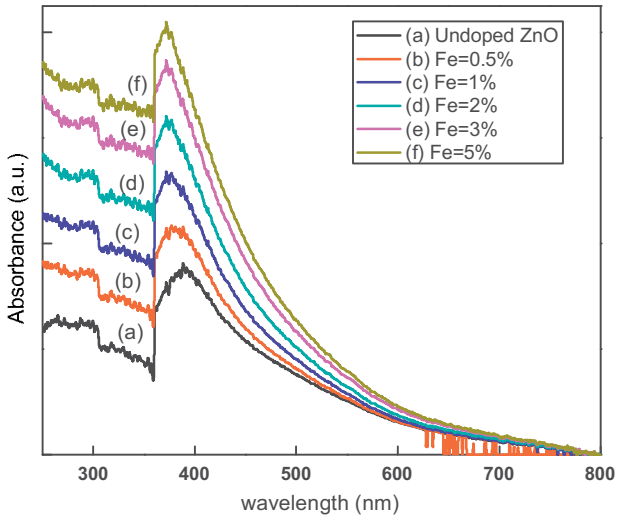

Fig. 9. UV–Visible absorption spectrum of Fe doped ZnO nanopowder.

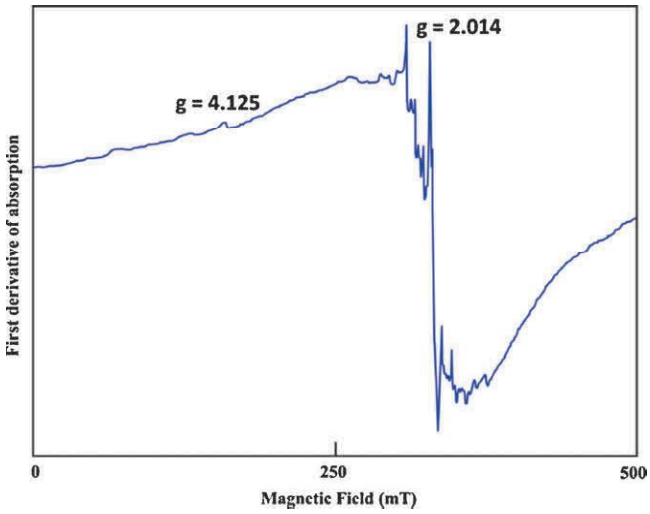

Fig. 11. EPR spectrum of ZnO:Fe (1 mol%) sample at room temperature.

Fe doped ZnO samples respectively. These E_g values are smaller than that of bulk ZnO (3.37 eV). In general, the absorption edges of nanoscale materials show a blue shift and their band gaps enlarge compared with the bulk due to quantum size effect.

In the present work, the reason for the band gap narrowing may originate from the introduction of Fe dopant. Diouri et al. [22] attributed the band-gap decrease of transition-metal ion doped II–VI semiconductors to the sp–d spin-exchange interactions between the band electrons and the localized d electrons of the transition-metal ion substituting the cation. The potential fluctuation introduced by ionised impurities leads to the band tailing of the valence band and conduction bands and contributes to the band gap narrowing. The electron–electron and electron–impurity interactions also could lead to the lowering of conduction band and upward shift of valence band. For low concentration of Fe doping, the reduction in the band gap has been theoretically explained as a consequence of exchange interaction between d electrons of the transition metal ions (Fe) and the host s and p electrons [23].

3.6. Electron paramagnetic resonance studies

Fig. 11 shows the EPR spectrum of $Zn_{1-x}Fe_xO_{(1+0.5x)}$ sample at room temperature. The EPR spectrum exhibits an intense resonance signal with effective g values at $g \approx 2.0$ with a sextet hyperfine structure (hfs) besides a weak resonance signal at $g \approx 4.13$. In addition to the above resonance signals a sharp resonance signal at $g \approx 2.014$ which is close to free electron value ($g = 2.0023$) is also observed and is generally attributed to an unpaired electron trapped on an oxygen vacancy site. The EPR spectrum suggests that in addition to Fe dopant a small amount of Mn impurity is also present in the sample. For d^5 transition metal ions (e.g. $Mn^{2+}$and Fe^{3+}), the axial distortion of octahedral symmetry gives rise to three Kramers' doublets $|\pm 5/2>$, $|\pm 3/2>$ and $|\pm 1/2>$ [24]. Application of a Zeeman field lifts the spin degeneracy of the Kramers' doublets. As the crystal field splitting is normally much greater than the Zeeman field, the resonances observed are due to transitions within the Zeeman field split Kramers' doublets. The resonance at $g \approx 4.13$ can arise from the transition between the energy levels of middle Kramers' doublet. The resonance at $g \approx 4.13$ can be attributed to the rhombic surroundings of the Fe^{3+} ions where as the resonance at $g \approx 2.0$ can be attributed to an environment close to tetrahedral symmetry and is known to arise from the transition between the energy levels of the lower doublet. The resonance signal at $g \approx 2.0$ exhibits six line hyperfine lines which is attributed to Mn^{2+} ions for which $S = I = 5/2$ and the hyperfine structure lines corresponding to the transition $(\frac{1}{2} \leftrightarrow -\frac{1}{2})$ fine-structure. Besides this, forbidden doublets corresponding to $\Delta m_I = \pm 1$ is also observed.

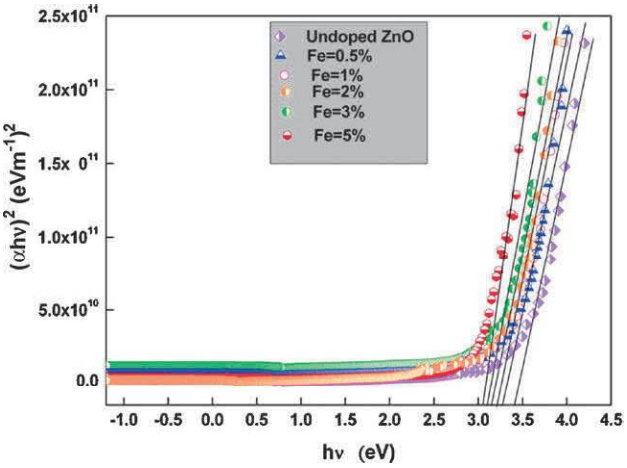

Fig. 10. Band gap of Fe doped ZnO nanopowder.

3.7. Photoluminescence studies (PL)

PL spectroscopy is an important tool to characterize the optical properties of a semiconductor. PL intensity may be directly correlated with the defect density in a nanomaterial. The room temperature PL spectrum of Fe doped ZnO sample excited with UV light source (325 nm) is shown in Fig. 12. For undoped ZnO sample, four emission peaks appears at 406, 420, 446, 484 and 520 nm. The peak near 406 nm arises due to violet emission whereas other two peaks belong to blue emission. For the ZnO nanoparticles, majority donors for luminescence in the visible region can be attributed to structural defects such as (Zn_i & O_i), vacancies (V_o & V_{zn}) and surface traps [25,26].

As can be seen from the figure, all the Fe doped ZnO samples show a dominant emission peak around 370 nm. This peak in the UV region is typically observed in nanocrystalline ZnO materials and has been assigned to the near band edge emission, since the energy corresponding to this peak is almost equal to the band gap energy of bulk ZnO. A close look at figure reveals a blue shift of UV peak positions in the Fe doped samples which confirm the incorporation of Fe in ZnO structure. The shift in the UV emission peak to lower energy in Fe doped samples is consistent with the UV–visible

Table 3
The kinetic parameters for ZnO:Fe nanomaterial estimated from Chen's glow peak shape method.

Peak T_m (°C)	Order of kinetics (b)	Activation energy E (eV)			
		E_τ	E_δ	E_ω	E_{ave}
314	0.51 (2)	1.27	1.29	1.29	0.34
342	0.51 (2)	3.02	2.83	2.94	0.89
359	0.47 (2)	4.62	6.27	4.54	1.43
370	0.49 (2)	9.16	8.01	8.60	2.81

absorption spectrum shown in Fig. 9. Further, the PL intensity of the UV peaks of Fe doped ZnO decreases with increase of Fe content. The intensity of the other broad luminescent peak observed around 467 nm increases a little with increase of Fe dopant. This can be assigned to the intrinsic defects particularly interstitial zinc [27].

3.8. Thermoluminescence (TL)

Thermoluminescence is now become a routine technique for measuring ionizing radiations. For this purpose, a number of commercially available TL dosimeters are used in the last three decades [28–31]. In the last one decade nanomaterials in radiation dosimetry find wide application in as-formed and doped with rare earth and transition metal ions doped in various host materials [32,33]. It has been established that luminescence properties of nanomaterials which are different from bulk entities. These studies clearly indicated potentiality of the nanosized materials in dosimetry of ionizing radiations where the conventional microcrystalline materials do not meet the desired requirements [34].

Fig. 13 shows the TL glow curves of γ-irradiated (1–5 kGy) nanocrystalline ZnO: Fe(2 mol%) at a warming rate of 6.7 °C s^{-1} recorded at RT. A well resolved glow peak at 368 °C was recorded in all the samples. Further, the structure of the glow curves is not much affected with variation of Fe dopant into the lattice. The TL intensity of the main glow peak is plotted against gamma dose (Inset of Fig. 13). It is found that the TL intensity increases with γ-dose. This increase in dose over wide range of dose in nanomaterials can be explained on the basis of Track Interaction Model (TIM). According to this model, the number of generated traps by high irradiation in a track depends mainly on cross sectional and length of the track inside the host matrix. In case of nanomaterials, the length of the track generated by high energy irradiation is of the order of few tenths of nanometers. As the dose increases, the TL intensity increases as still some nanoparticles exist that would have missed while being targeted by the high energy irradiation, owing to the small size of the particles. This gives good linearity over a wide range of dose [35]. The glow curve is related to the trap levels that lie at different depths in the band gap between the conduction and valence bands of a solid. These trap levels are characterized by different kinetic parameters. The kinetic parameters such as activation energy, order of kinetics are evaluated after deconvolution of broad glow curve. In the present studies, a broad single peak without any inflection points indicating the existence of overlapped peaks. Therefore, the deconvolution was done using origin software

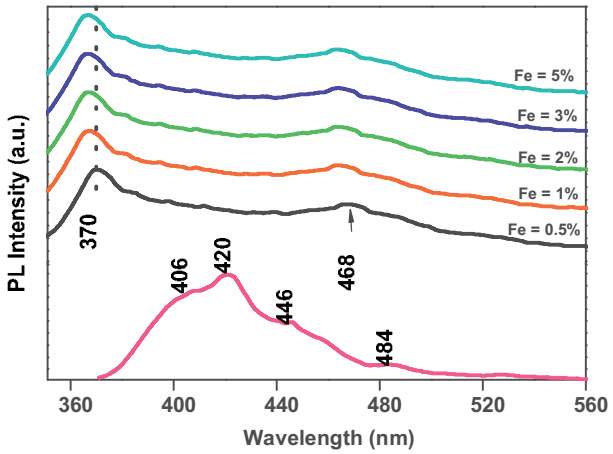

Fig. 12. PL emission spectrum of Fe doped ZnO nanopowder.

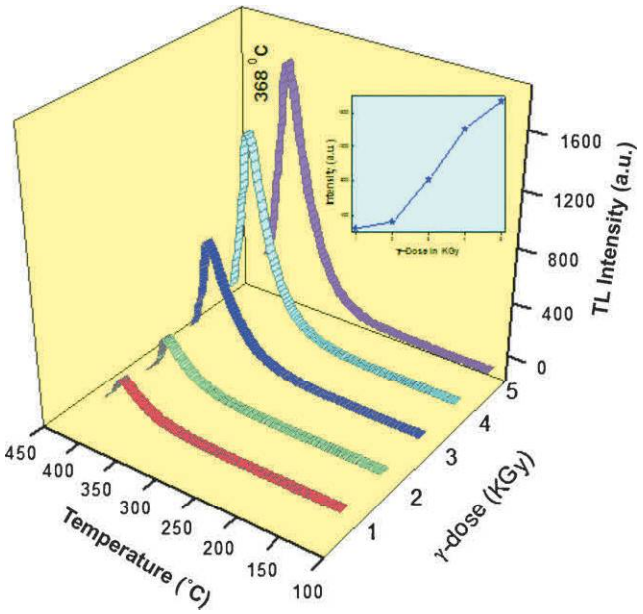

Fig. 13. TL glow peaks of ZnO:Fe (2 mol%) at different γ-ray doses (1–5 kGy).

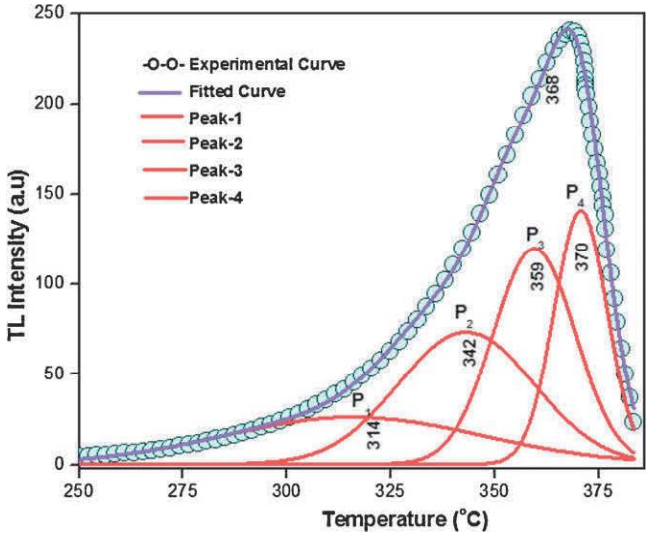

Fig. 14. A typical glow curve for ZnO:Fe (2 mol%) nanocrystalline phosphor after 1 kGy gamma exposure at a heating rate of 6.7 °C s^{-1}.

8.0 version for all the Fe doped samples for estimation of kinetic parameters. Fig. 14 shows the deconvoluted glow curve for ZnO: Fe (2 mol%) exposed to1kGy. The deconvoluted glow peaks were used to estimate the parameters using Chen's peak shape method and the obtained values are given in Table 3. The average activation energy (E_{ave}) was found to be in the range 0.34–2.81 eV. This wide thermal activation energy range might be due to extension of band gap of ZnO: Fe nanomaterial has been observed in several nanomaterials.

4. Conclusions

Low-temperature solution combustion method has been successfully used to synthesize Fe doped ZnO nanoparticles. From PXRD results, single phase pure hexagonal wurtzite structure is observed. SEM and TEM images reveal quasi-hexagonal morphology of the nanoparticles. In samples with higher Fe doping concentration, the porous nature is dominated. This is due to large amount of gases escaping during combustion process. The optical band gap E_g is found to decrease with increase of Fe dopant concentration. This is due to exchange interaction between d electrons of the transition metal ions (Fe) and the host s and p electrons. From Raman studies, the active modes observed at 100, 438, 332, 580 cm^{-1} correspond to pure ZnO. In Fe doped samples, two nonpolar optical phonon (E_2) modes at low and high frequencies at 100 and 435 cm^{-1} are observed. These modes broaden and disappear with increase of Fe dopant concentration. The EPR spectrum suggests that in addition to Fe dopant a small amount of Mn impurity is also present in the sample. A single well resolved thermoluminescent glow peak at ~368 °C was observed in all the Fe doped samples. The TL intensity is found to increase with increase of gamma dose which is one of the desired properties of TL dosimeter.

Acknowledgements

Dr. B.M. Nagabhushana gratefully acknowledges Visvesvaraya Technological University, Belgaum, for the financial support (VTU/2009-10/A-9/11714) to carryout this research work. Prof. J.L. Rao is highly thankful to University Grants Commission (New Delhi) for the award of Emeritus Fellowship.

References

[1] J.D. Holmes, K.P. Johnston, R.C. Doty, Science 287 (2000) 1471–1473.
[2] M.H. Huang, S. Mao, H. Feick, Science 292 (2001) 1897–1899.
[3] X.Y. Kong, Z.L. Wang, Nano Lett. 3 (2003) 1625–1631.
[4] Y. Tak, K. Yong, J. Phys. Chem. B 109 (2005) 19263–19269.
[5] X.D. Wang, C.J. Summers, Z.L. Wang, Nano Lett. 4 (2004) 423–426.
[6] S. Kolenisk, B. Dabrowski, J. Mais, J. Appl. Phys. 95 (2004) 2582–2586.
[7] M. Purica, E. Budianu, E. Rusu, M. Danila, R. Gavrila, Thin Solid Films 403 (2002) 485–488.
[8] Z.M. Dang, L.Z. Fan, S.J. Zhao, C.W. Nan, Mater. Sci. Eng. B 99 (2003) 386–389.
[9] J.Y. Lao, J.G. Wen, Z.F. Ren, Nano Lett. 2 (2002) 1287–1291.
[10] P.G. Li, W.H. Tang, X. Wang, J. Alloys Compd. 479 (2009) 634–637.
[11] Y. Li, G.W. Meng, L.D. Zhang, F. Phillipp, Appl. Phys. Lett. 76 (2000) 2011–2013.
[12] S. Yamabi, H. Imai, J. Mater. Chem. 12 (2002) 3773–3778.
[13] J.J. Kingsley, K.C. Patil, Mater. Lett. 6 (1988) 427–432.
[14] S. Ekambaram, Y. Iikubo, A. Kudo, J. Alloys Compd. 433 (2006) 237–240.
[15] J. Rodrigueg-carvajal Fullprof.2000. A program for Rietveld, Profile matching and integrated intensity refinements for X-ray and neutron data. Version 1.6 Laboratorie Leon, Brillounin, Gifsuryvette, France, 2009.
[16] G.K. Williamson, W.H. Hall, Acta Metall. 1 (1953) 22–31.
[17] X. Sui, Y. Liu, C. Shao, Y. Liu, C. Xu, Chem. Phys. Lett. 424 (2006) 340–344.
[18] Khan A. Alim, Vladimir A. Fonoberov, Manu Shamsa, Alexander A. Balandin, J. Appl. Phys. 97 (2005) 124313.
[19] B.C. Cheng, Y.H. Xiao, G.S. Wu, L.D. Zhang, Appl. Phys. Lett. 84 (2004) 416.
[20] M.C. Klein, F. Hache, D. Ricard, C. Flyzanis, Phys. Rev. B 42 (1990) 11123–11136.
[21] Sofer, D. Sedmidubsky, S. Huber, J. Hejtmanek, M. Marysko, K. Jurek, M. Mikulics, J. Cryst. Growth 314 (2011) 123–128.
[22] J. Diouri, J.P. Lascaray, M. El Amrani, Phys. Rev. B 31 (1985) 7995.
[23] R.B. Bylsma, W.M. Becker, J. Kossut, U. Debska, D. Yoder-Short, Phys. Rev. B 33 (1986) 8207–8215.
[24] A. Abragam, B. Bleaney, Electron Paramagnetic Resonance of Transition Ions, Clarendon, Oxford, 1970.
[25] J.C. Johnson, H.Q. Yan, P.D. Yang, R.J. Saykally, J. Phys. Chem. B 107 (2003) 8816–8828.
[26] D. Stichtenoth, C. Ronning, T. Niermann, L. Wischmeier, T. Voss, C.J. Chien, P.C. Chang, J.G. Lu, Nanotechnology 18 (2007) 435701–435705.
[27] Z. Fang, Y. Wang, D. Xu, Y. Tan, X. Liu, Opt. Mater. 26 (2004) 239–242.
[28] T. Nakajima, Y. Murayama, T. Matsuzawaand, A. Koyano, Nucl. Instrum. Methods Phys. Res. B 157 (1978) 155–162.
[29] A. Aypar, H. Demirta, J. Appl. Radiat. Isotopes 36 (1985) 566–568.
[30] A.J.J. Bos, Nucl. Instrum. Methods Phys. Res. B 184 (2001) 3–28.
[31] Y.S. Horowitz (Ed.), Thermoluminescent and Thermoluminescent Dosimetry, vol. 1/3, 1, CRC Press, Boca Raton, FL, 1984.
[32] S.W.S. McKeever, Thermoluminescence of Solids, Cambridge University Press, Cambridge, 1985.
[33] A. NecmeddinYazici, M. Ozatas, M. Bedir, Opt. Mater. 29 (2007) 1091–1096.
[34] Numan Salah, P.D. Sahare, S.P. Lochab, Pratik Kumar, Radia. Measur. 41 (2006) 40–47.
[35] Y.S. Horowitz, O. Avila, M. Rodrigues-Villafuerte, Nucl. Instrum. Methods Phys. Res. B 184 (2001) 85–122.